
Analysis of cylindrically and spherically embossed flux barriers in non-oriented electrical steel

Ines Moll*^a · Simon Vogt^a · Tobias Neuwirth^b ·
Benedikt Schauerte^c · Kay Hameyer^c · Michael
Schulz^b · Alex Gustschin^b · Wolfram Volk^a ·
Hannes Alois Weiss^a

^a Technical University of Munich, Chair of Metal Forming and Casting, Walther-Meißner-Str. 4, 85748 Garching, Germany

^b Technical University of Munich, Heinz Maier-Leibnitz Zentrum (MLZ), Lichtenbergstr. 1 85748 Garching, Germany

^c RWTH Aachen University, Institute of Electrical Machines (IEM), Schinkelstr. 4, 52062 Aachen, Germany

Received: date / Accepted: date

Abstract In reluctance and permanent magnet synchronous machines, flux barriers are crucial for magnetic flux guidance. Designed as cutouts, flux barriers reduce the mechanical strength of the rotor construction. To operate these electric drives at higher rotational speed, an alternative flux barrier design is required. Since residual stress influences the magnetic properties of soft magnetic materials, this paper deals with embossing induced residual stress as flux barriers in non-oriented electrical steel with 2.4 wt% silicon and a sheet thickness of 0.35 mm. The investigated flux barriers were fabricated with a cylindrical or spherical punch at two different penetration depths and were compared to a flux barrier fabricated as cutout. A residual stress analysis using Finite Element Analysis helps understanding the mechanism of embossed flux barriers. Additionally, the influence of induced residual stress on the magnetic material behavior is measured using standardized single sheet tests and neutron grating interferometry measurements. This investigation aimed at a better understanding of the flux barrier design by local induction of residual stress.

Keywords Electric drive, Electrical steel, Magnetic flux barrier, Embossing, Imprint, Residual stress

1. Introduction

With politics emphasizing energy change, the significance of energy efficiency is increasing. One factor to enhance the energy efficiency of electric drives, especially of reluctance and permanent magnet synchronous machines, is optimizing the magnetic flux guidance in the electrical steel that form the motor core. Conventionally, cutouts are inserted in electrical steel sheets for magnetic flux guidance. Coincidentally, they deteriorate the mechanical strength of the rotor construction. Hence, the maximum rotational speed of the motor is limited. The following investigation focus on an alternative strategy of magnetic flux guidance in electrical steel to enable higher rotational speed and to increase the power density of electric drives.

Prior studies revealed that mechanical stress has a negative effect on the magnetic properties of non-oriented electrical steel [1]. The inverse magnetostrictive effect describes the correlation between mechanical stress and magnetic material

behavior. These studies focused on the effect of mechanical stress caused by dynamic loads, like centrifugal forces [2], or of processing induced residual stress, e.g. by blanking [3], on the magnetic properties of non-oriented electrical steel. Their target was the decrease of the magnetic deterioration by reduction of mechanical stress. It is determined, that compressive residual stress has a higher impact on the magnetic material behavior than tensile residual stress [1, 4].

In contrast, the following work aims to enhance the properties of electric drives by focused application of the inverse magnetostrictive effect. As residual stress deteriorates the magnetic material behavior, the local induction of residual stress reduces the magnetic permeability in the affected volume, hence the magnetic flux. As shown in [5] this phenomenon allows a magnetic flux guidance.

Different to [5], the relation between residual stress distribution and magnetic material behavior is analyzed in detail. Furthermore, the influence of cylindrical and

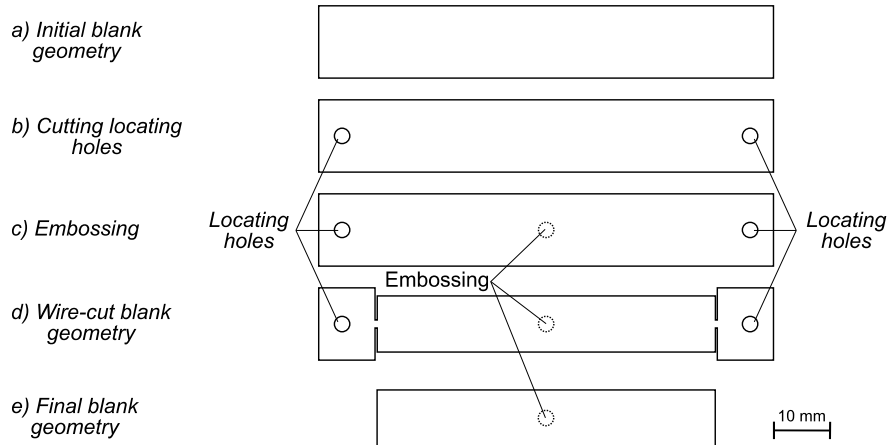


Fig. 1 Schematic illustration of specimen manufacturing: a) initial blank geometry, b) cutting of locating holes, c) embossing of flux barrier, d) wire-cutting and e) final blank geometry.

spherical embossing geometries and of different penetration depths is examined. To evaluate the relation of embossing and magnetic properties, it is crucial to quantify the distribution of residual stress with a Finite Element Analysis (FEA) of the embossing process. The magnetic material behavior of the specimen is analyzed with neutron grating interferometry (nGI) [6] and single sheet tests [7]. Additionally, the functionality of the embossed flux barrier is demonstrated by comparing it to a flux barrier fabricated as cutout. This investigation is necessary to show the applicability of the new flux barrier design for electric drives.

2. Methods

2.1 Specimen manufacturing process

The specimens were fabricated from a non-oriented electrical steel with a silicon content of 2.4 wt% and a sheet thickness of 0.35 mm, comparable to [5]. The size of 10 mm x 60 mm has been maintained, because it is suitable for both magnetic measurement methods. The strategy of specimen manufacturing is illustrated in Fig. 1. In the first step, locating holes are cut in the specimen and the flux barrier is embossed. Secondly, the final specimen geometry is wire-cut. To finish the specimen manufacturing, the final specimen geometry is measured optically.

To begin, two locating holes are cut in the specimen with the same punching tool used for embossing (Fig. 1 b). The locating holes are mandatory to ensure a reproducible position of the embossing in the specimen's center.

Subsequent, the specimens are positioned with the locating holes and the magnetic flux barriers are embossed with a cylindrical or spherical punch (Fig. 1 c). The two exemplary punch geometries were selected, because of strongly varying deformations and residual stress distributions. The tool, which is schematically shown in Fig. 2, is designed like a shear cutting tool. The main components are embossing punch, die and blank

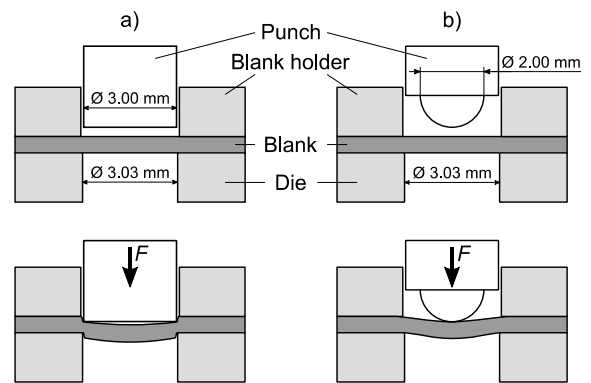


Fig. 2 Schematic illustration of the embossing tool and the embossing of the blank with a), cylindrical punch, and b), spherical punch.

holder. The blank holder ensures that the blank keeps its position during embossing. For the embossing, two different punches were selected. One embossing punch has a spherical tip with a diameter of 2.00 mm, while the second embossing punch has a cylindrical tip similar to a punch used for shear cutting with a diameter of 3.00 mm. The cylindrical die remains unchanged for all experiments and has a diameter of 3.03 mm. The tool was utilized on a servo press with a velocity of 30 strokes per minute. The tool concept and the deformation of the blank caused by the punch force F is illustrated in Fig. 2.

The embossing depth, i.e. the way the punch penetrates below the initial upper surface of the blank, is adjustable. This allows a variation of the deformation grade between different embossings, which is for the executed experiments between 36 μm and 240 μm . With the cylindrical embossing punch and a sufficient penetration depth, the electrical steel sheet can be shear cut to produce a specimen with cutout as flux barrier.

Tab. 1 Measured final depth of deformation between initial blank surface and center of deformation as well as corresponding simulated penetration depths.

Specimen	Punch	Resulting embossing depth (mm)	Simulated penetration depth (mm)
Cyl - PD 1	Cylindrical	0.031	0.036
Cyl - PD 2	Cylindrical	0.235	0.240
Sph - PD 1	Spherical	0.073	0.079
Sph - PD 2	Spherical	0.225	0.230

Succeeding, the final specimen geometry is produced (Fig. 1 d). The contour, shown in Fig. 1, is wire-cut. This cutting method ensures a negligible influence of the cut edges on the magnetic properties of the specimen [8]. Hence the cutting of the specimen doesn't need to be considered for the simulation of residual stress. During the wire-cutting, the specimens are positioned and fixed over the locating holes. Finally, the additional parts on both sides of the specimens are removed (Fig. 1 e).

To finish the specimen production, the obtained embossing geometry is analyzed. A 3D-scan of the specimen's surface was executed with a confocal laser scanning microscope to analyze the final deformation and the penetration depth.

The specimen names are combined of the used punch, *Cyl* for cylindrical and *Sph* for spherical punch, and the penetration depth, *PD 1* for a small penetration depth and *PD 2* for a higher penetration depth. The sample names and the resulting depth of embossing are listed in Tab. 1.

2.2 Finite element analysis

The embossing process is computed to analyze the relation between residual stress distribution in the specimen and its magnetic material behavior. The flux barrier caused by a cutout is not accounted in the FEA as Weiss et al. [9] analyzed the effect of cutting in greater depth. With the Finite Element Analysis (FEA), a three-dimensional numerical model calculates the embossing related deformation and mechanical stress in the specimen. The embossing process is structured in three steps: clamping the blank with blank holder, embossing with cylindrical or spherical punch and removing external forces on the specimen to allow a springback movement.

To clamp the blank, a blank holder force of 25.5 kN is applied. Next, the punch penetrated the electrical steel. The depth varies because of different final depths of the specimens' embossings, which are listed in Tab. 1. Completing the numerical analysis, the springback of the blank is simulated: all external forces on the specimen are removed concurrent with punch, blank holder and die. The final geometry after step three is compared to the optically measured specimen profile to iteratively adapt the penetration depth. Thus obtaining a model close to reality. The computed stress without

influence of external mechanical forces results in the required residual stress distribution.

The geometric parameters of the numerical model are approximately the same as in the experimental setup, see chapter 2.1. The edge radius of the die and the cylindrical punch are set to 0.05 mm.

The non-oriented electrical steel is an approximately homogenous material with slightly different properties in and transverse to rolling direction. Considering the small anisotropy and the symmetry of the embossing process, calculating a quarter of the model is sufficient and reduces the computation time. The deformation of the tools is neglected due to modelling them as rigid bodies.

The material model is built on the measurement of material properties in [9]. The edge lengths of the elements, which are used for the discretization of the blank, are between 0.0017 mm in areas with high deformations and 2.58 mm in areas with small deformations. The mesh consists of 37870 8-node linear brick C3D8R elements for the embossing simulation with cylindrical punch and 46823 elements for the model with spherical embossing geometry.

As tensile and compressive residual stress have a different influence on the magnetic properties of electrical steel, von Mises equivalent stress criterion is not applicable for the analysis. A distinction of tensile and compressive residual stress is realized by the analysis of local maximum absolute principle stress $\sigma_{\max, \text{principle, abs}}$.

The stress values are evaluated along lines intersecting the specimen perpendicular to the blank surface. For each line 350 stress values are analyzed over the sheet thickness and separated in tensile and compressive stress. Subsequent, the mean tensile and compressive stress is computed for the line. The evaluation lines are arranged in a distance of 5 μm along five cross sections intersecting the center of embossing. Each cross section is rotated in an angle of 22.5°. The residual stress distributions of the cross sections were averaged to a single residual stress distribution plotted to the distance x from the center of embossing. Because of symmetry constraints, the residual stress distribution in and transverse to rolling direction are included with weighting factor 0.5 to the mean residual stress distribution.

Tab. 2 Magnetization of specimen in nGI-measurements: applied electric currents I and resulting magnetic field strength H .

Applied current I (A)	0.00	0.47	1.34	2.00	3.00	4.00	5.00	6.67
Magnetic field strength H (A/m)	0.00	780	2230	3330	4955	6660	8325	11105

2.3 Experimental methods

2.3.1 Neutron grating interferometry

The imaging method neutron grating interferometry (nGI) analyzes the absorption, phase shift and ultra-small-angle neutron scattering (USANS) of a neutron beam passing through the specimen. [10] Neutrons do not interact with the electron hull, but the atomic core. This allows for a high penetration in most metals i.e. electrical steel. Due to their spin, neutrons also interact with magnetic fields. In the case of a magnetic domain structure, as found in electrical steels, the scattering of the neutrons is in the USANS regime. These two factors cause nGI to be the prime technique to analyze local magnetic properties in bulk samples.

The image containing information about USANS is called the dark field image (DFI). Encoded in the DFI is information about the local magnetic domain structure, which in turn is linked to the residual stress distribution in the evaluated volume. [6]

The neutron grating interferometer used for this study is a Talbot-Lau interferometer for neutrons [11]. A detailed explanation of the components and principle of a neutron grating interferometer may be found in [11] and [12].

The measurements were performed at the neutron imaging beamline ANTARES at the FRM II [13, 14]. As experimental setting, a correlation length of $1.865 \mu\text{m}$ was selected. The exposure time of 10 s and an amount of 30 images per sample resulted in a total exposure time of 300 s per nGI-scan. The used detector has a field of view of $70.3 \text{ mm} \times 83.3 \text{ mm}$. The pixel size is $32.5 \mu\text{m} \times 32.5 \mu\text{m}$ and the achieved resolution is roughly $90 \mu\text{m}$.

The measurement of the specimens was conducted under the influence of different magnetic fields to analyze the effect of magnetization on the behavior of magnetic flux barriers. The yoke, described in [15] induces the magnetic field in the specimens, which is generated by an electric current in the coils. In Tab. 2, the applied electrical currents I and resulting magnetic field strengths H are listed.

For evaluation of the DFI-signal, the measurement results were normalized to the DFI-signal of a virgin reference specimen. A scaled DFI-signal lower than 1 signifies a higher magnetic domain density and a value higher than 1 a lower magnetic domain density, compared to the reference. To analyze the progression of the magnetic domain structure, the scaled DFI-signal

of all pixels at discrete distances of the embossing's center were radially averaged.

The magnetic domain structure of a specimen is highly affected by the residual stress. Additionally, the local magnetic domain structure gives an idea of the movement of magnetic domains under magnetization. The movability and magnetizability of magnetic domains are fundamental for the global magnetic properties.

2.3.2 Single sheet tests

Single sheet measurements are used for magnetic property characterization of electrical steel averaged across the entire volume of specimens. The measurement system utilized for this work is a double yoke $60 \text{ mm} \times 60 \text{ mm}$ single sheet tester (SST). The specimen is clamped in between two yokes which close the magnetic circuit. The influence of the reluctance return path for the flux in the yokes can be neglected because of the considerably larger cross section of the yoke when compared to the specimen. The specimen is surrounded by two windings. The primary winding applies the magnetic field strength. The secondary winding induces the measurement voltage and thus the magnetic flux density in the specimen. The electrical currents in the primary windings are controlled in such a way, to cause sinusoidal magnetic flux density waveforms with a predefined amplitude B_m at a magnetization frequency f . In this way, the specimen can be compared in terms of characteristic properties such as iron loss, magnetic permeability and hysteresis loop shape [16].

For the selected measurement system, a specimen's geometry of $60 \text{ mm} \times 60 \text{ mm}$ is optimal. Its size is reduced to $60 \text{ mm} \times 10 \text{ mm}$ for this study, to measure the identical specimen as analyzed in the nGI. The specimen is clamped centrally between the yokes. The magnetic field and the resulting flux density are measured simultaneously and recorded, when a sinusoidal magnetic flux density waveform is set up in the investigated volume. For the measurements, a magnetization frequency f of 50 Hz was selected. The magnetic flux density is the average of the measured magnetic flux across the specimen's cross section. The magnetic field can be calculated by the known magnetic path length, number of turns of the primary winding and the electrical current in the excitation coil.

A magnetic flux density exists between the yokes even without specimen due to the permeability of the vacuum μ_0 , the so-called air flux. It is considered by air

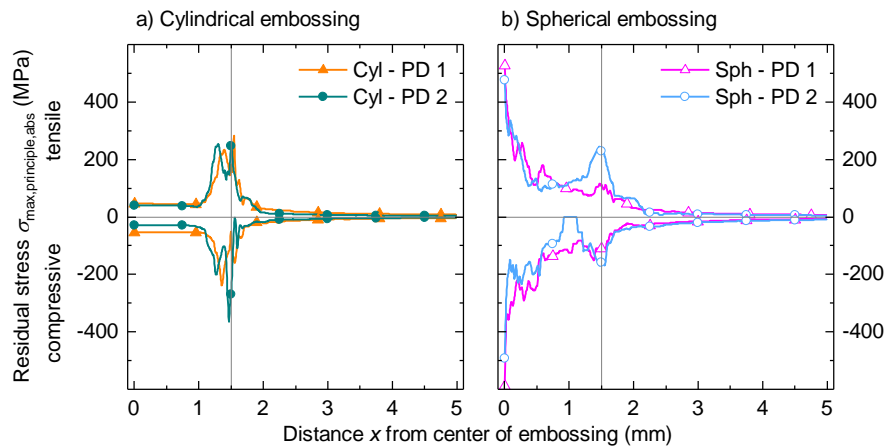


Fig. 3 Numerically analyzed distribution of tensile and compressive residual stress $\sigma_{max,principle,abs}$ plotted to the distance x from center of embossing for a), the cylindrically embossed specimens, and b), the spherically embossed specimens.

flux compensation to solely measure the magnetic flux in the specimen.

By principle, the single sheet tests only enable a conclusion on the global magnetic material behavior without insights on the local distribution of the magnetic flux. The combination of nGI and SST is necessary to analyze the magnetic material behavior of the embossed flux barriers. The connection of global magnetic properties and numerically analyzed local residual stress is shown in [17] by analyzing electrical steel in a tensile test.

3. Results

3.1 Numerical analysis of residual stress

The following part depicts and discusses the FEA results of the embossing process. In Fig. 3, the simulated residual stress distributions distinguished into tensile and compressive stress are displayed. The vertical line at distance $x = 1.5$ mm represents the position of die diameter equal to the edge of embossing.

For the cylindrically embossed flux barriers, the maximal tensile and compressive residual stress values appear at a distance close to 1.5 mm. A higher penetration depth leads to a larger maximum of compressive residual stress at punch and die diameter and to a lower tensile and compressive stress level in- and outside of the embossing.

The simulated residual stress distributions of the spherically embossed flux barriers show global tensile and compressive stress maxima in the center of the embossing and local maxima at distance $x = 1.5$ mm. The local compressive stress maxima are significantly smaller than the global ones of the cylindrically embossed specimen. For Sph - PD 2, the local maximum of the tensile stress is two times the one of Sph - PD 1 and has a similar magnitude as the global tensile stress maxima of the cylindrical embossings. The

residual stress outside the spherical embossings are increased in relation to the cylindrical embossings.

In summary, a higher total residual stress amount is induced using the spherical punch. The maxima of the spherical embossing are higher than the ones of the cylindrically embossed specimens. Additionally, the residual stress outside and inside the spherical embossing is more increased compared to the cylindrically embossed flux barrier.

3.2 Local magnetic material behavior

The effect of residual stress on the local magnetic domain structure of the specimens was determined using neutron grating interferometry. The scaled DFI of the cylindrically and spherically embossed specimens are displayed in Fig. 4. They were fabricated with high penetration depth and measured with an applied magnetic field strength H of 780 A/m. The results of the embossed flux barriers are compared to the specimen with a flux barrier fabricated as cutout (Fig. 4 c). The lowest scaled DFI-signals are measured at the edge of the cylindrical, in the center of the spherical embossing and on the right and left side of the cutout. The scaled DFI-signal is strongly increased above and below the cylindrical embossing and the cutout. This effect slightly occurs in the spherically embossed specimen.

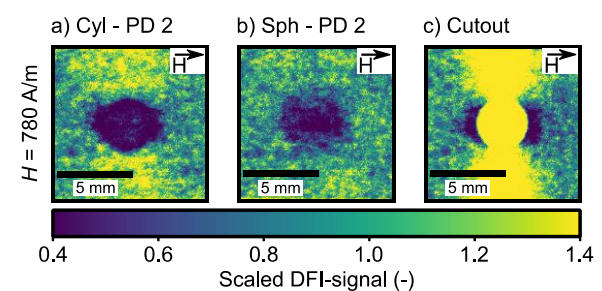


Fig. 4 Scaled DFI of a), Cyl - PD 2, and b), Sph - PD 2, with applied magnetic field strength H of 780 A/m.

For further evaluation, the scaled DFI-signal progression of the cylindrically embossed specimen are compared to the specimen with cutout (Fig. 5). Close to the cutting line, the magnetic material behavior of this specimen is affected by shear cutting [15]. This causes an increased amount of magnetic domains close to the cutout. For the cutout flux barrier, the magnetic domain density in the remaining material is slightly decreased when compared to the reference material because the same magnetic flux is concentrated to a smaller cross section. Hence, the applied magnetic field strength has a higher impact on the remaining material.

The cylindrically embossed flux barriers show a scaled DFI-signal slightly higher than 1 outside of the embossing, similar to the cutout. At the edge of the embossing, the scaled DFI-signal is characterized by a minimum, which is lower for higher penetration depths. Embossing Cyl - PD 1 has a scaled DFI-signal above 1 in the center of embossing. In contrast, the scaled DFI-signal of embossing Cyl - PD 2 is only slightly increased from the edge to the center of embossing. The difference of minimal value of the scaled DFI-signal from small to high magnetization is approximately 0.5 for Cyl - PD 1 and lower than 0.25 for embossing Cyl - PD 2. Thus, the embossed flux barrier Cyl - PD 2 is more stable and has still an effect of flux guidance at high magnetic field strengths. Deductively, the cylindrically embossed flux

barrier has a higher impact on the magnetic domain density in the center of the embossing, if the grade of deformation is sufficient. This is achieved with embossing Cyl - PD 2.

The minimal scaled DFI-signal of the spherically embossed specimen is located in the embossing's center and increases up to a distance of 3 mm, see Fig. 6. The scaled DFI-signals for the whole distance from the center of embossing is lower than 1, consequently more magnetic domains are measured in the evaluated volume than in the reference specimen, except of the measurement results at a magnetic field strength of 780 A/m. Therefore, the magnetic material behavior of the spherically embossed specimen is degraded in the full evaluated volume. The scaled DFI-signal is slightly lower for the specimen fabricated with higher penetration depth. The minimal scaled DFI-signal at the highest magnetization compared to the lowest magnetization increases by 0.5. Due to that, the influence of spherical embossings on the magnetic domain structure is more dependent on the magnetization compared to Cyl - PD 2.

In summary, the difference between Sph - PD 1 and Sph - PD 2 is far smaller than between the cylindrical embossings. The spherically embossed specimens have the highest amount of magnetic domains in the embossing's center. For cylindrical embossings the

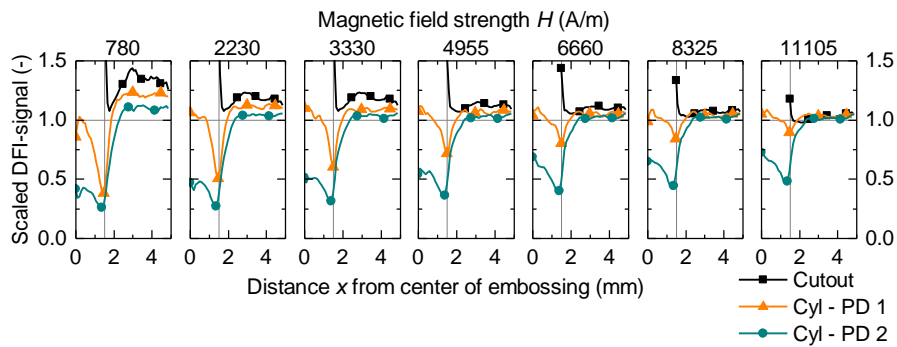


Fig. 5 Scaled DFI-signal of the cylindrically embossed specimens at two different penetration depths compared to a specimen with a cutout (diameter 3.00 mm) as flux barrier measured at different magnetic field strengths H .

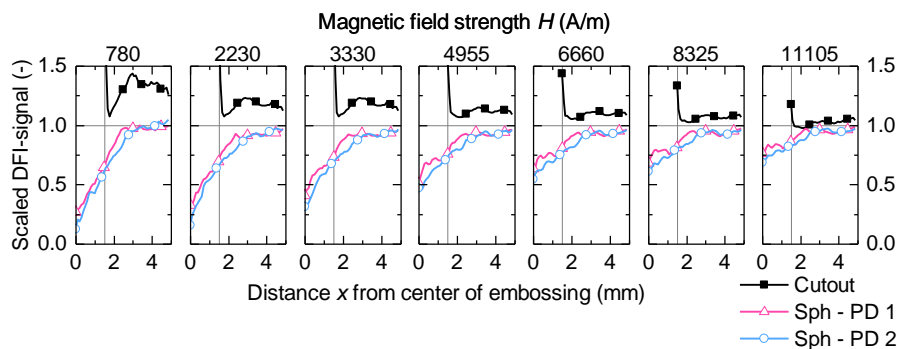


Fig. 6 Scaled DFI-signal of the spherically embossed specimens at two different penetration depths compared to a specimen with a cutout (diameter 3.00 mm) as flux barrier measured at different magnetic field strengths H .

minimal scaled DFI-signal is located at distance 1.5 mm. The magnetic material behavior of the spherically embossed specimens is additively deteriorated outside the embossed part. The effect on the magnetic domain structure decreases for higher magnetizations. For the two penetration depths, the difference of the scaled DFI-signal progression is small. A concentrated effect on the magnetic material behavior in the area of embossing is detected for the cylindrically embossed flux barriers. Outside the embossing less magnetic domains are measured compared to the reference. At increased magnetic field strength, the effect of the embossing Cyl - PD 2 on the magnetic domain structure is still considerably high in contrast to the other specimens.

3.3 Global magnetic material behavior

The global magnetic properties, iron loss, magnetic permeability and hysteresis loop shape, of the embossed specimen and the reference material were analyzed with single sheet tests. Because the embossing has the highest impact on the permeability, this is the eligible parameter to illustrate the effect of embossed magnetic flux barriers. The comparison to the reference material

shows the deterioration of the magnetic properties by the embossings.

In Fig. 7, the magnetic permeabilities of the embossed specimens fabricated with small penetration depth are compared to a higher penetration depth. The embossing of flux barriers reduces the permeability of electrical steel compared to the reference material. A cylindrical embossing with a penetration depth of 36 μm has a slightly smaller magnetic material deterioration compared to the penetration depth of 240 μm for magnetic flux densities lower than 1 T. For a magnetic flux density above 1.3 T, the permeability of Cyl - PD 2 is higher than the one of the reference material. Above 1.4 T, the permeability of Cyl - PD 1 and the reference material are approximately the same.

The permeability of spherically embossed specimens is further reduced for higher penetration depth. For magnetic flux densities above 1.3 T, the magnetic permeability of the spherically embossed electrical steel results in values higher than the ones of the reference. This effect only occurs in a comparatively small scope of magnetic flux densities, but has to be analyzed in further studies.

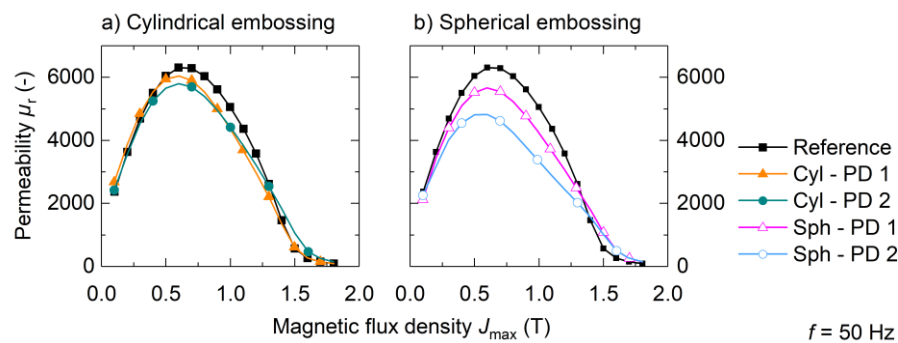


Fig. 7 Magnetic permeability μ_r for a), cylindrically embossed, and b), spherically embossed specimen, fabricated with two different penetration depths compared to a reference material.

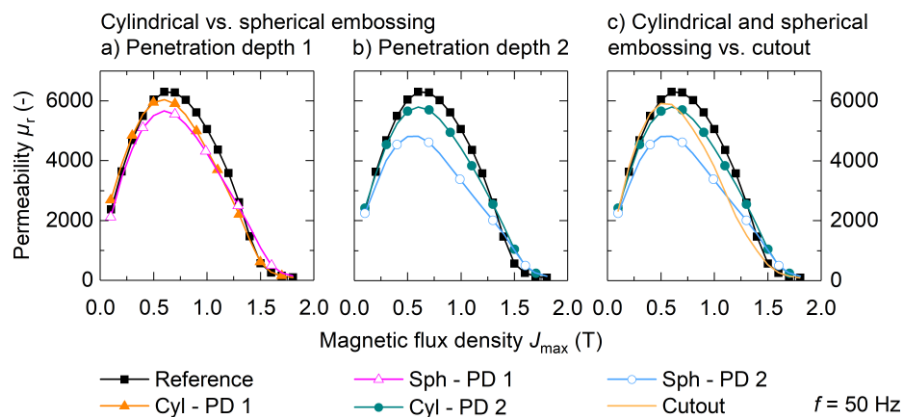


Fig. 8 Magnetic permeability μ_r of cylindrically and spherically embossed specimen fabricated with a), penetration depth 1, and b), with penetration depth 2, compared to reference material and c), comparison of reference material, cylindrically embossed specimen with a penetration depth of 240 μm , spherically embossed specimen with a penetration depth of 230 μm and flux barrier manufactured as cutout.

The permeabilities of spherically and cylindrically embossed specimen are compared in Fig. 8 a) and Fig. 8 b). For small penetration depths and low magnetization, the permeability of the spherical embossing is further reduced. At high magnetic flux densities, the cylindrically embossed specimen shows weakly increased magnetic deterioration. Fig. 8 b) distinguishes the permeability of the different embossing geometries at penetration depth 2. Sph - PD 2 has a reduced permeability compared to the cylindrically embossed specimen.

To show the effect of embossed flux barriers, the results of Cyl - PD 2 and Sph - PD 2 are compared to a flux barrier fabricated as cutout (Fig. 8 c). The permeability of Sph - PD 2 is up to 1.3 T strongly reduced compared to the specimen with cutout. Up to a magnetic flux density of 0.7 T, the permeability of the specimen with the cutout is slightly higher than the one of Cyl - PD 2. As shown in Fig. 5, the magnetic domain density of Cyl - PD 2 at the edge of embossing is higher than the one of the specimen with cutout. Hence, the embossing magnetically deteriorates an enlarged volume. For magnetic flux densities above 0.7 T, the permeability of Cyl - PD 2 is increased compared to the specimen with cutout, because the magnetic flux can partially pass the embossed flux barrier and has therefore a larger cross section. In summary, the cylindrically embossed flux barrier Cyl - PD 2 has almost the same influence on the permeability of the specimen like a cutout with similar geometry, if the magnetic flux density is lower than 0.7 T.

4. Discussion

Connecting the numerical analysis with the magnetic measurements, a causal relationship between residual stress distribution and magnetic properties is apparent. For the interpretation of the averaged residual stress

distribution, the knowledge of an higher impact on the magnetic material deterioration of compressive stress compared to tensile stress is essential [1]. To illustrate the relation of residual stress distribution and magnetic domain structure, the results are combined in Fig. 9. The diagrams of the nGI were measured with a magnetic field strength of 4955 A/m.

The stress peaks at distance 1.5 mm of the cylindrical embossings lead to an increased magnetic domain density (Fig. 9 a). Despite small residual stress inside the embossings, the magnetic domain density is still at an increased level. The cylindrical flux barrier design results in a flux barrier shaped as circle, which adds up to a reduced magnetic flux inside the embossed circle. Inducing lower tensile residual stress (Cyl - PD 1) weakly affects the magnetic domain structure inside the embossing, especially at high magnetic flux densities.

As the residual stress in- and outside of Cyl - PD 1 are a bit higher than the stress values of Cyl - PD 2, the magnetic permeability is further reduced (Fig. 7 a). To conclude, strongly increased compressive residual stress in a restricted material volume has a higher impact on the magnetic flux guidance than peaks of tensile residual stress, even on the material volume in the embossing, which only has slightly increased residual stress.

In the center of the spherical embossing, the highest stress values and a maximum amount of magnetic domains arise (Fig. 9 b). The residual stress outside the embossing as well as the amount of magnetic domains is increased in relation to the cylindrically embossed specimens. Hence, a larger volume is mechanically and magnetically deteriorated. Comparing both spherical embossings, the mean stress are similar (Fig.). The slightly increased magnetic domain density approves

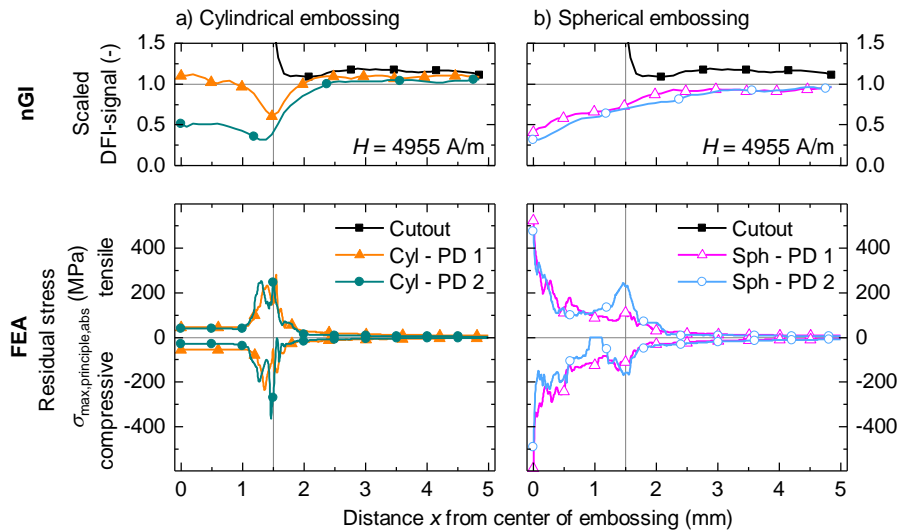


Fig. 9 Comparison of scaled DFI-signal at a magnetic field strength H of 4955 A/m and numerically analyzed residual stress distributions $\sigma_{max,principle,abs}$ of a), cylindrical, and b), spherical embossings.

the reduced permeability of Sph - PD 2 (Fig. 6 and Fig. 7).

To compare the cylindrical and spherical embossings, the focus is set on penetration depth 2, because the embossings Cyl - PD 1 and Sph - PD 1 are fabricated with strongly deviating penetration depths. The residual stress and the magnetic domain density outside of the embossed geometry are increased for Sph - PD 2 (Fig. 9). The magnetic domain density in embossing Cyl - PD 2 is slightly smaller than the maximal density of Sph - PD 2 but affects a larger volume and has a stronger effect at higher magnetic field strength. Thus the embossing Sph - PD 2 has locally a higher impact on the magnetic properties but weakly influences the material outside the center of embossing. The spherical embossing deteriorates the magnetic properties up to a distance of 5 mm. These results substantiate the decreased permeability of Sph - PD 2 (Fig. 8).

Finally, Cyl - PD 2 and Sph - PD 2 are compared to a specimen with a cutout (diameter 3 mm) to analyze its effect as flux barrier Fig. 8 c). The spherically embossed specimen has a considerably reduced permeability compared to the specimen with cutout. At low magnetizations, the permeability of the cylindrically embossed specimen is slightly smaller than the permeability of the specimen with cutout. At higher magnetic flux densities the permeability is above the one of the specimen with cutout (Fig. 8). High magnetizations allow the magnetic flux to partially pass the embossed flux barrier, which is not possible for the cutout, and the permeability is increased. In summary, focused induced residual stress has the potential to guide magnetic flux, especially at magnetic flux densities below 0.7 T for the investigated embossed specimen.

5. Conclusions

This work studied the effect of focused induced residual stress by cylindrical and spherical embossing on the magnetic flux guidance in electrical steel. With the FEA, the residual stress distribution in the specimen was numerically computed. The magnetic properties were evaluated locally by neutron grating interferometry and globally by single sheet tests. The magnetic domain structure and the resulting magnetic permeabilities were approved by the computed residual stress distribution. A large amount of compressive residual stress (Cyl - PD 2) has a sustainable effect on the magnetic domain structure in the embossed geometry. This is achieved by cylindrical embossing. The spherical embossing led to a stress maximum in the embossing's center and higher residual stress up to a distance of 5 mm. The spherical flux barrier has no determined boundaries like the cylindrical embossing. Hence, the global magnetic properties of the spherically embossed specimen are more deteriorated than the ones of the cylindrical embossing.

Summarizing, the magnetic flux guidance by locally induced residual stress was approved, especially by the

comparison to a flux barrier fabricated as cutout. Further investigations have to define optimal residual stress distributions and suitable embossing geometries for the application of focused induced residual stress as flux barrier. Furthermore, the increased permeabilities of the embossed specimen compared to the virgin reference material measured at magnetic flux densities above 1.3 T have to be analyzed.

6. Acknowledgements

This work was supported by the Deutsche Forschungsgemeinschaft (DFG) in the DFG priority program "SPP2013 – Focused Local Stress Imprint in Electrical Steel as Means of Improving the Energy Efficiency" - HA 4395/22-1; SCHU 3227/2-1; VO 1487/31-1. The results of this work are based upon experiments performed at the ANTARES instrument at Heinz Maier-Leibnitz Zentrum (MLZ), Garching, Germany.

7. References

1. Naumoski H, Maucher A, Herr U (2015), Investigation of the influence of global stresses and strains on the magnetic properties of electrical steels with varying alloying content and grain size. doi:10.1109/EDPC.2015.7323206
2. Cao H, Huang S, Shi W (2019), Influence of core stress on performance of permanent magnet synchronous motor. *Journal of Magnetics* 24(1):24–31. doi:10.4283/JMAG.2019.24.1.024
3. Weiss HA, Trober P, Golle R, Steentjes S, Leuning N, Elfgen S, Hameyer K, Volk W (2018), Impact of Punching Parameter Variations on Magnetic Properties of Nongrain-Oriented Electrical Steel. *IEEE Transactions on Industry Applications* 54(6):5869–5878. doi:10.1109/TIA.2018.2853133
4. Kai Y, Tsuchida Y, Todaka T, Enokizono M (2014), Influence of biaxial stress on vector magnetic properties and 2-D magnetostriction of a nonoriented electrical steel sheet under alternating magnetic flux conditions. *IEEE Transactions on Magnetics* 50(4). doi:10.1109/TMAG.2013.2287875
5. Vogt S, Neuwirth T, Schauerte B, Weiss HA, Falger PM, Gustschin A, Schulz M, Hameyer K, Volk W (2019), Extent of embossing-related residual stress on the magnetic properties evaluated using neutron grating interferometry and single sheet test. *Production Engineering* 13(2):211–217. doi:10.1007/s11740-018-0863-7
6. Grünzweig C, David C, Bunk O, Dierolf M, Frei G, Kühne G, Kohlbrecher J, Schäfer R, Lejcek P,

- Rønnow HMR, Pfeiffer F (2008), Neutron decoherence imaging for visualizing bulk magnetic domain structures. *Physical Review Letters* 101(2). doi:10.1103/PhysRevLett.101.025504
7. British Standards Institution (1992), Magnetic materials. Methods of measurement of the magnetic properties of magnetic sheet and strip by means of a single sheet tester (6404-3). British Standards Institution. doi:10.3403/00279002. Zugegriffen: 10. January 2020
 8. Kurosaki Y, Mogi H, Fujii H, Kubota T, Shiozaki M (2008), Importance of punching and workability in non-oriented electrical steel sheets. *Journal of Magnetism and Magnetic Materials* 320(20):2474–2480. doi:10.1016/j.jmmm.2008.04.073
 9. Weiss HA, Leuning N, Steentjes S, Hameyer K, Andorfer T, Jenner S, Volk W (2017), Influence of shear cutting parameters on the electromagnetic properties of non-oriented electrical steel sheets. *Journal of Magnetism and Magnetic Materials* 421:250–259. doi:10.1016/j.jmmm.2016.08.002
 10. Strobl M, Grünzweig C, Hilger A, Manke I, Kardjilov N, David C, Pfeiffer F (2008), Neutron dark-field tomography. *Physical Review Letters* 101(12). doi:10.1103/PhysRevLett.101.123902
 11. Neuwirth T, Backs A, Gustschin A, Vogt S, Pfeiffer F, Böni P, Schulz M (2020), A high visibility Talbot-Lau neutron grating interferometer to investigate stress-induced magnetic degradation in electrical steel. *Scientific Reports*
 12. Reimann T, Mühlbauer S, Horisberger M, Betz B, Böni P, Schulz M (2016), The new neutron grating interferometer at the ANTARES beamline: Design, principles and applications. *Journal of Applied Crystallography* 49(5):1488–1500. doi:10.1107/S1600576716011080
 13. Calzada E, Gruenauer F, Mühlbauer M, Schillinger B, Schulz M (2009), New design for the ANTARES-II facility for neutron imaging at FRM II. *Nuclear Instruments and Methods in Physics Research Section A: Accelerators, Spectrometers, Detectors and Associated Equipment* 605(1-2):50–53. doi:10.1016/j.nima.2009.01.192
 14. Schulz M, Schillinger B (2015), ANTARES: Cold neutron radiography and tomography facility. *JLSRF* 1. doi:10.17815/jlsrf-1-42
 15. Weiss HA, Steentjes S, Tröber P, Leuning N, Neuwirth T, Schulz M, Hameyer K, Golle R, Volk W (2019), Neutron grating interferometry investigation of punching-related local magnetic property deteriorations in electrical steels. *Journal of Magnetism and Magnetic Materials* 474:643–653. doi:10.1016/j.jmmm.2018.10.098
 16. Fiorillo F (2004), Measurement and characterization of magnetic materials, 1. Aufl. Elsevier series in electromagnetism. Elsevier Academic Press, San Diego, Calif. [u.a.]
 17. Leuning N, Steentjes S, Weiss HA, Volk W, Hameyer K (2018), Magnetic Material Deterioration of Non-Oriented Electrical Steels as a Result of Plastic Deformation Considering Residual Stress Distribution. *IEEE Transactions on Magnetics* 54(11). doi:10.1109/TMAG.2018.2848365